Published by
NIGERIAN SOCIETY OF PHYSICAL SCIENCES
Available online @ https://asr.nsps.org.ng/index.php/asr

African Scientific Reports 4 (2025) 205

African Scientific Reports

# Aspect ratio of thermo-hydraulic performance of periodically prescribed semi-circular groove in rectangular channel

Samson A. Aasa*, Regan K. Dunne, Dawood A. Desai

*Department of Mechanical and Mechatronic Engineering, Faculty of Engineering and the Built Environment, Tshwane University of Technology, South Africa*

## Abstract

A rectangular channel including an angled groove on the end wall was modeled in an air tunnel to assess the augmentation of heat transfer and the friction factor. The groove exhibited a 45-degree angle relative to the flow direction, with a pitch-to-groove depth ratio of 6.5. Three distinct aspect ratios, 0.025, 0.03, and 0.05, were evaluated. The Reynolds number varied from 1000 to 11000, including laminar to turbulent flow regimes. The pressure reduction and thermal transfer were quantified in the primary flow of the experimental portion. The 0.05 aspect ratio yielded the highest performance, with optimal values of 22%, 30%, and 48% in the laminar, transition, and turbulent areas, respectively. The non-dimensional air temperature of the flow at the conclusion of the test portion demonstrated the dispersion of the fluid, signifying uniform turbulence within the channel. The impacts of various plate factors on enhancing heat transmission were regulated. This was ascribed to the channel aspect ratio, mild pressure penalties, and the significant thermal increases of the groove endwalls. It reduced the thickness of the fluid layer at the surface, facilitated prolonged smooth flow over the groove surfaces, and is essential for enhancing the efficiency and sizing of flat plate heat exchangers in applications such as solar panels, fuel cells, electronic components, motor/generator jackets, bearing jackets, and turbine blades. The findings indicated that angled grooves can be beneficial in several contemporary applications, including turbine blades, solar cells, and processing equipment.

DOI:10.46481/asr.2025.4.3.205

*Keywords:* Convective heat enhancement, Artificial technique, Semi-circular groove, Friction factor, Nusselt number

*Article History :*
Received: 30 April 2024
Received in revised form: 23 July 2025
Accepted for publication: 25 July 2025
Published: 22 December 2025



## 1. Introduction

The cooling scheme of the interior components of modern applications is central to the effectiveness of the heat exchanger devices. Different shapes used in things like turbine blades, solar panels, fuel cells, and photovoltaic cells have increased the lifespan of these parts by improving their performance and working conditions. Moreover, studies on flow structure have produced positive outcomes by pinpointing gaps in the majority of geometries used in heat enhancement parameters and techniques [1, 2]. Sharma *et al.* [3] and Salawu *et al.* [4] carried out studies on fluid enhancement done in nanofluid for convective heat exchanger devices. Undoubtedly, more researchers are studying the properties and effects of these parameters using various techniques [5–8]. The key parameters in this category include the depth, space, pitch, nature, and orientation of the turbulators, and they are observed to have

*Corresponding author Tel. No.: +27-74-428-7015.
*Email address:* aasa.samson@oouagoiwoye.edu.ng (Samson A. Aasa)

tremendous effects on the thermal enhancement of a system [1, 2]. These parameters are recognized as significant when passive technique geometries are used. The performance of devices is greatly affected by these parameters' impact on the heat exchanger and cooling jacket channels of various machine parts. Using different methods to enhance the inside of the heat exchanger, like pin fins, ribs, bumps, and wire mesh, has helped make the system work better and last longer. However, this submission has its challenges of high-pressure penalties, which often affect the efficiency of the systems, Arik and Bunker [5]. Pressure challenges encountered by using increased rough surfaces, fins, and inserts to increase the convective heat transfer coefficient have always been a subject of discussion [6, 7]. This study critically examines the engagement of the grooved surface in a rectangular air channel to enhance its thermal performance. The technique is important because of its merits, which are generally adjudged to combine the positivity of both cylindrical and dimple geometries with a rough surface endwall. Unlike the other techniques, it supports low-pressure penalties, no thermal bond contact, and ease of manufacturing.

The pressure penalty resulting from rough surfaces had been well-documented in various studies on grooves and other rough surfaces [9, 10]. Bilen *et al*. [11] studied the effect of three different geometries in heat enhancement analysis on turbine vanes. The computational analysis employed ANSYS to simulate the effects of the various performance parameters. It was discovered that the U-duct with a 45° angle gave the highest heat transfer, while the U-duct with ribs and a simple U-duct contributed the lowest convective heat transfer. Lee *et al*. [12] used both arc- and rectangular-groove-shaped channels to investigate the heat transfer numerically within Re of 10,000–30,000. The optimum groove geometries were revealed, and the thermophysical properties and points on the groove where the highest heat flux occurred were analyzed. Furthermore, the arc-shaped grooved channel demonstrated the highest enhancement during deep heat transfer. In addition, Refs. [2, 11, 13] studied the performance parameters of local heat transfer and flow hydrodynamics. Xie *et al*. [13] numerically investigated the thermal performance in microchannels using different grooves and obstacles by implementing characteristics of field synergy performance. The test facility measured 200 $\mu$m (H) and 50 $\mu$m (W). The diameter and depth of the grooves and obstacles were 100 $\mu$m, and the depth was 20 $\mu$m. The experiment was performed within a Reynolds number of 100-900. Based on the arrangements of grooves and obstacles, the results revealed that $Nu/Nu_o$ and $f/f_o$ range from 1.446 – 26.19 and 0.18 – 110.19, respectively. Grooves showed excellent performance compared to other established geometrics, according to the literature. This is because it combines the features of dimples and circular configurations, which are known for moderate pressure penalties in flow-heat enhancement.

In addition, other studies had investigated the potential of grooved channels in fluid flow structures. Eiamsa-ard and Promvonge [14] established that groove-walled turbulators provide optimum thermal performance using various simulated models, and related investigations in Ref. [15] further support the effectiveness of such configurations. At an orientation angle of 45°, they achieved an approximately 58% improvement in convective heat transfer. The analysis in Refs. [16, 17] identified a primary flow structure that provides additional support for the previously reported enhancements in the thermal performance of grooves. Therefore, groove turbulators are preferred because they provide better performance with relative penalties. Moreover, the improved effectiveness owing to increasing fluid turbulence, generation of secondary fluid flow patterns, and convection mixing could not be overemphasized. Studies have shown that further work is required for a more effective thermal performance of modern technology that is saddled with high energy consumption and heat dissipation. To achieve improved thermal enhancement, various rough surfaces (grooves) arranged 45° to the plane surface were applied. The irresistible advantage of combining dimples and cylindrical geometrical roughness attributes on flows made semi-circular grooves non-contestable geometries [18]. In addition, the colossal amount of heat generated by the working exceeds the metallurgical limit of the material parts, and high-penalty turbulence agents like protrusions, inserts, and pin fins do not perform effectively at low Reynolds numbers, leading to ineffective heat transfer.

The use of groove turbulence promoters has been established to achieve high heat enhancement with a moderate pressure drop, noncontact effects with heat transfer surfaces, and excellent bonded internal fins. Thus, the present study presents an operative scheme to enhance the convective heat transfer coefficients in a rectangular air channel employing semi-circular grooves. The array of grooves was oriented at 45° relative to the mean flow direction and was located on one side of the wall in the channel. Similarly, the groove is 1 mm in depth and 9 mm in pitch on a 500 mm × 203 mm rectangular channel. The pressure drops and local heat transfer coefficients were measured for three channel heights (7, 10 and 13 mm). The flow Reynolds number was varied to cover the laminar, transitional, and turbulent flow regimes. Smooth channel data were measured in the same channel to indicate the effects of the grooves. The enhancement of heat transfer with the pressure penalty is then presented to demonstrate the thermal performance of the grooved channel, as the Reynolds number is varied. The results will give engineers useful information to better design cooling channels used in solar panels, photovoltaic cells, fuel cells, electronic chips, motor casings, and flat plate heat exchangers for better heat management.

## 2. Material and methods

### *2.1. Experimental set-up*

Figure 1(a) shows a schematic of the experimental test facility used. It is a rectangular air channel with the following sections: the contraction zone of the 27:1 ratio two-dimensional section, a 0.5 m section of a 2 m long developing section before the test section (0.5 m) attached immediately after the developing flow section, and then it enters a 0.5 m long section before the plenum box. The air channel maintained a uniform rectangular cross-section that was adjustable to the desired height from the exit of the contraction

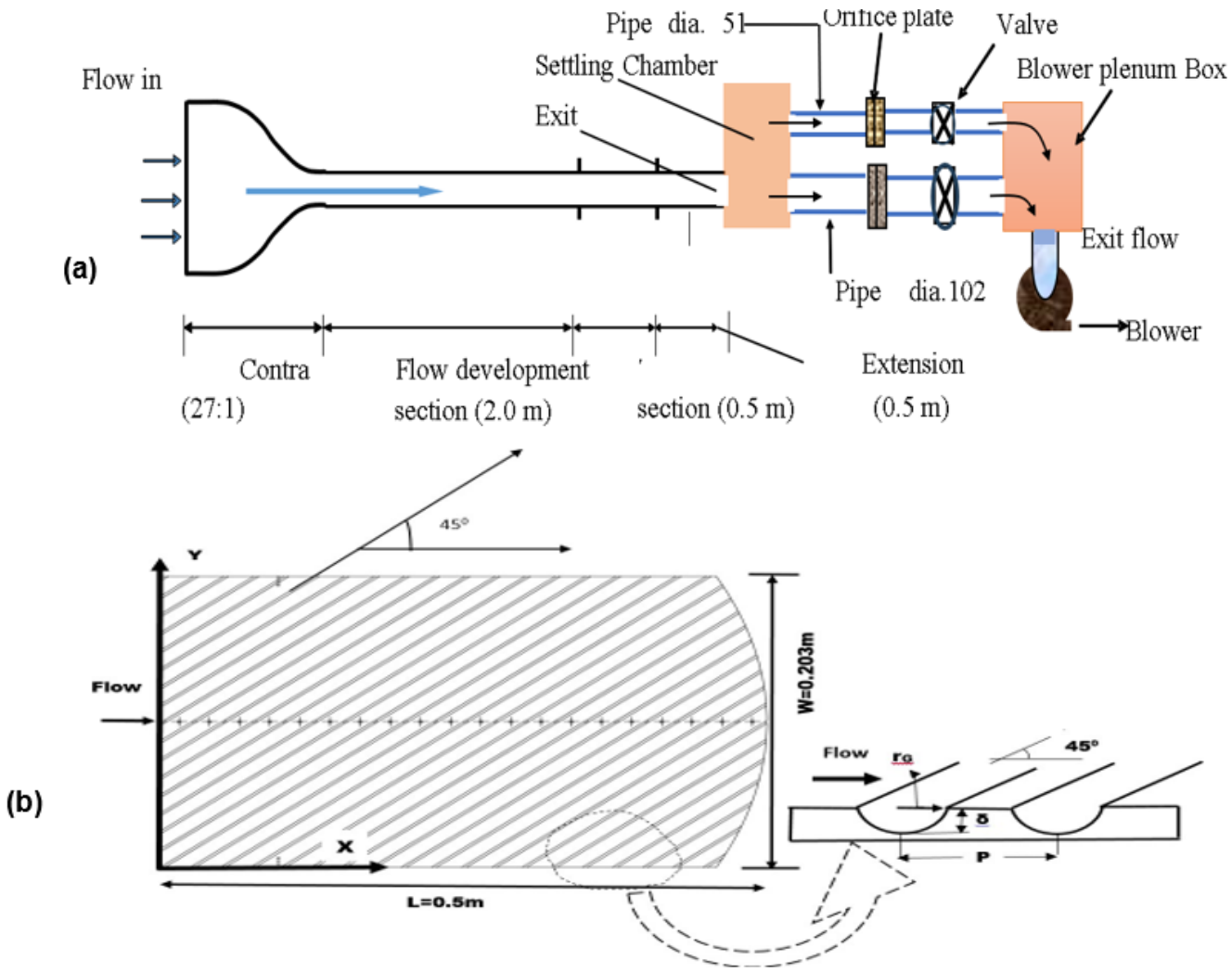


Figure 1. (a) Experimental setup of the wind tunnel. (b) Groove plate geometric details 45°.

section to the inlet of the plenum. A centrifugal blower, along with ambient laboratory air, draws the air through the channel and the test section. Commercial polycarbonate acrylic plastic, measuring 12 mm in thickness and 203 Ssmm in width, formed the channel walls. As shown, air from the plenum box flowed through the metered pipe sections connected to the blower. The ISO standard 5167-1980 [19] utilized orifice plates with beta ratios of 0.51 and 0.21, and small diameters of 0.05 m and 0.02 m for the 4- and 2-inch pipes, respectively. The pipe sections were connected to differential pressure transducers to determine the mass flow rate in the air channel. A variable speed drive was used to control the blower speed and mass flow rate. Sealants were used between the adjacent channel sections to prevent air leakage into the channels.

The pressure drop was acquired by tapping one side of the 203 mm walls of the test section with 0.3 mm and 1.5 mm (made to fit the tube diameter's external and internal diameters of 1.5 mm and 1 mm, respectively) stepped holes along the length. Thirty-three pressure taps were placed at equal intervals of 15 mm and scanned using a mechanical scanner. The pressure differences were then acquired using the already arranged plastic pressure tubes. The size of the heat transfer measurement plate was a pre-designed 203 × 500 × 6 mm polycarbonate acrylic plate suitable for smooth and groove channels. A thin layer of copper tape covered the heater to provide continuous heat flux to the airflow embedded with film heaters of Kapton™ tape-encapsulated Inconel heating elements [20, 21]. The side of the wall with the heaters had two layers of black insulation foam, 50 mm each. Figure 2(b) shows the heat transfer section and measurement coordinate systems for the study. The heated walls had thermocouples at the locations shown in Figure 2(a). Similarly, four thermocouples were located on both sides at regular intervals of 25 mm in the insulation layers. Through the drilled hole, wall thermocouples were placed on the grooved wall for surface temperature measurements. The insulation thermocouples provide temperature measurements to estimate conduction power losses from the heaters. Only the thermocouples were placed in contact with the wall heater in the downstream half of the plate, as shown in Figure 2(a).

Pressure drop measurements were obtained under ambient isothermal conditions, and the average convective heat flux determined

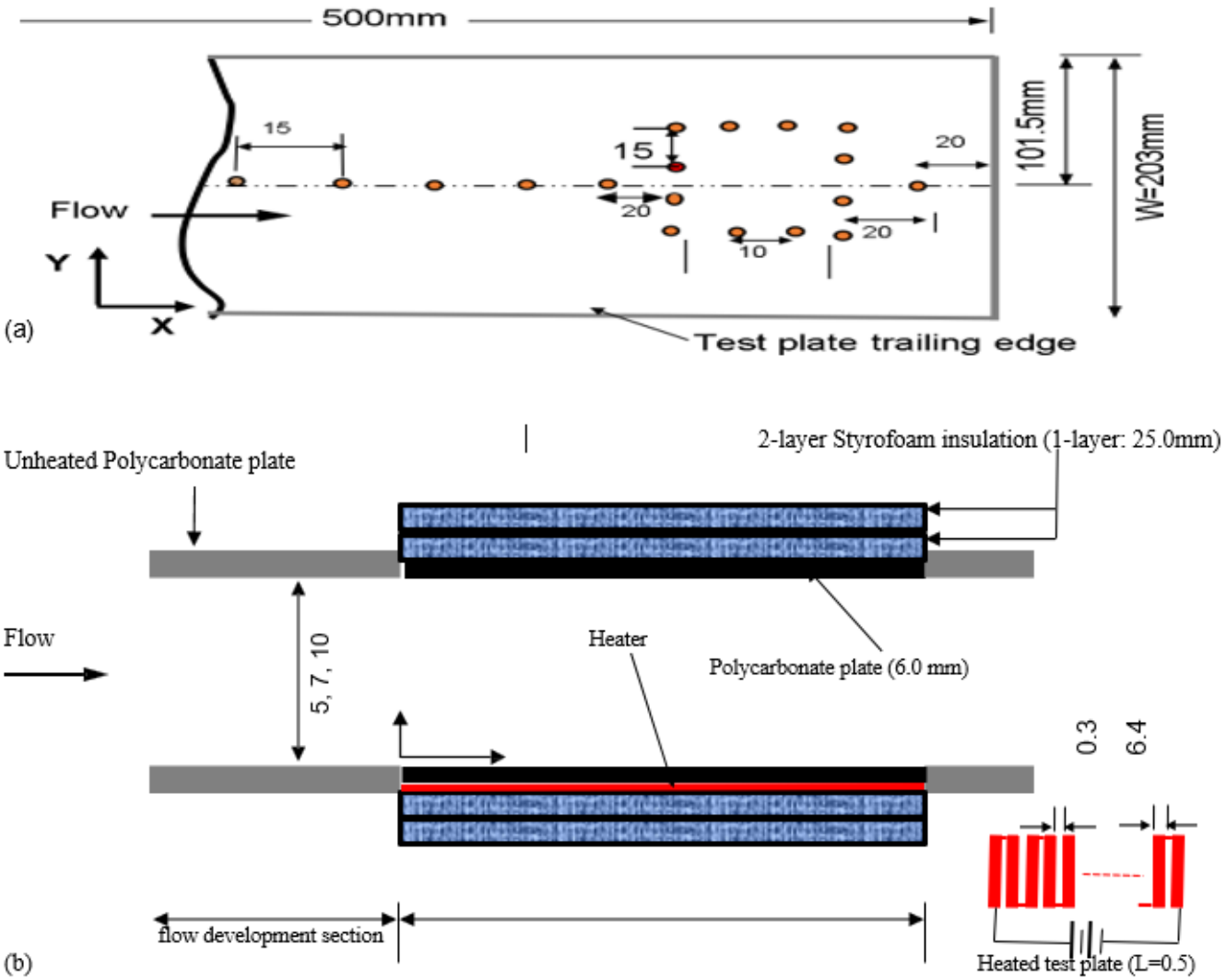


Figure 2. (a) Tc location along the test section (b) Heater's arrangement along the test section.

the heat transfer from each heated wall. The film heaters employed on the two walls have identical resistances and are in series. A single DC power source was used to ensure that the same power input level was used for the heaters. The signals from the pressure transducers and thermocouples were recorded using a National Instrument data acquisition system via a LabView computer program. The data from each acquisition channel were acquired at 500 Hz for 2 s for temperature and 100 Hz for 2 s for pressure. The signals were then time-averaged and converted into degrees Celsius and Pascal after applying the appropriate calibration curves. Based on Stolz's equation, the discharge coefficients of the orifice plates were determined in Ref. [22], using the orifice pressure difference through iterations. The ideal gas law was used to estimate the air density for the mass flow measurements. The thermal conductivity of air, ka, is calculated by averaging the temperature at the test section entrance, $T_{a,in}$, and the average temperature in the area, $T_{m,x}$. A thermocouple located at the test section inlet measured $T_{a,in}$. The energy balance in Eq. (1) was used to estimate the local $T_{m,x}$ along the test channel. The specific heat Cp in the is estimated at $T_{a,in}$ as the maximum difference of $(T_{w,x} - T_{a,in})$:

$$T_{m,x} = T_{a,\text{in}} + \frac{\sum Q_{c,x}}{m_a\, c_p}. \tag{1}$$

Figure 2(a) displays the heat transfer measurements obtained with the heated wall. For the groove surface, the heater was attached to the external wall of the grooves and insulated with a firm gridlock of insulated foams, and it was assumed that heat was transferred to the air stream with a small heat loss. Conduction analysis was then applied to determine the conduction loss using a one-dimensional method, as shown in Ref. [17]. The maximum loss was estimated to be 5% of the heat flux. The total convective power is negligible, as it is calculated by subtracting conduction loss from the heater's applied power and the heat due to radiation.

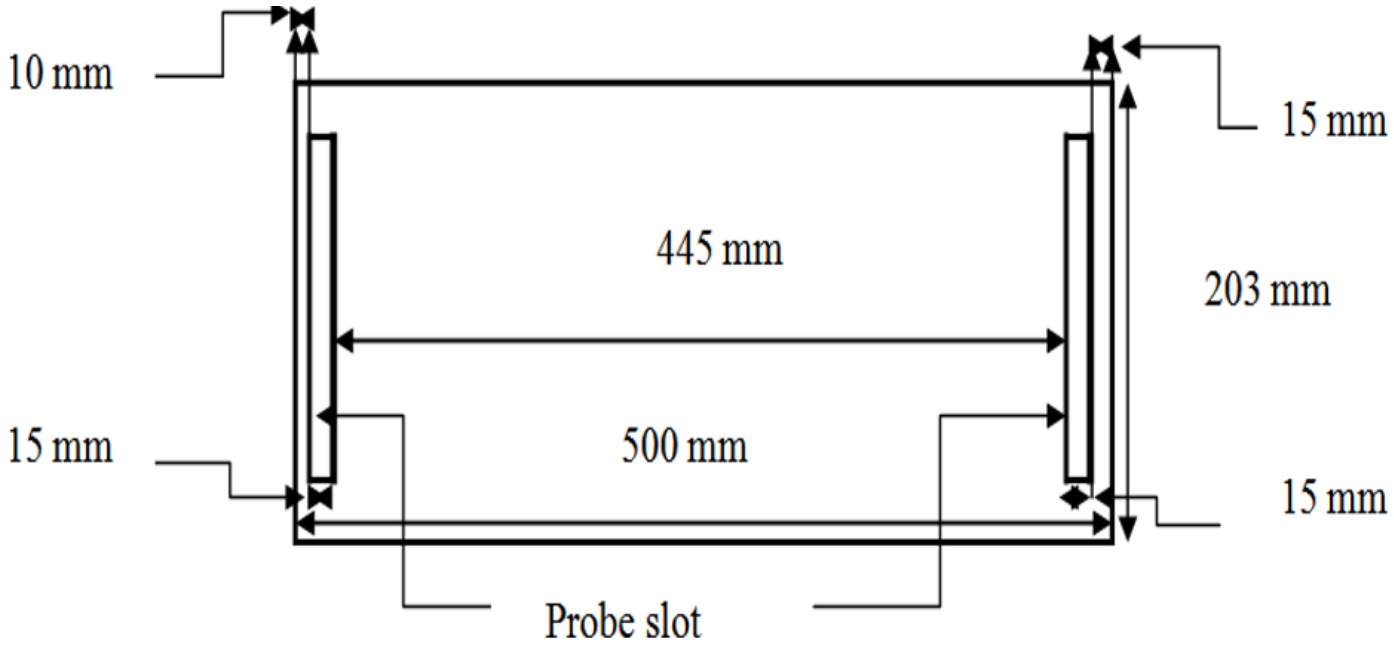


Figure 3. Air temperature slot at the top endwall.

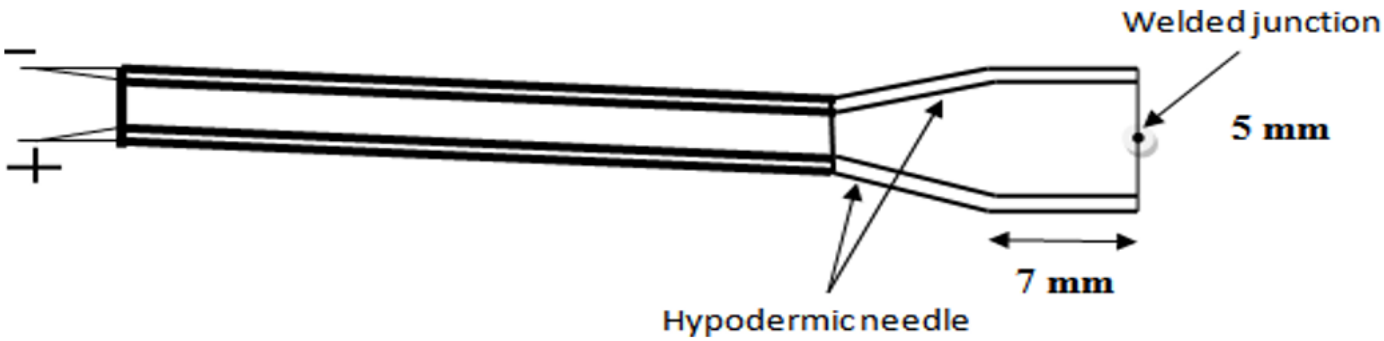


Figure 4. Air temperature distribution thermal probe.

The heat transfer was calculated using the local Nusselt number of the groove plate, Nux, for the thermocouple location, by applying the average convective heat flux $Q_c/(LW)$ on the test surface, as shown in Eq. (2). All measurements taken at the thermocouple position within the test section were with and without the groove. The fully developed Nusselt number, Nu0, measured in the smooth test section is 7% different in the laminar Re and less than 4% different in the turbulent Re compared to the calculated values in the smooth channel [17]. Using [22–24], the smooth channel correlation yielded a maximum difference of 5% for the measured friction factor, $f_0$

$$\mathrm{Nu}_x = \frac{Q_c\, D_h}{[(L\,W)\,(T_{w,x} - T_{m,x})\,K_a]}. \tag{2}$$

### 2.2. Semi-circular grooves geometry

Semicircular grooves were fabricated using a commercial CNC machine for accurate design purposes. The diameter for the groove print, Dp, and the center-to-center pitch, p, were 2 mm and 9 mm, respectively. The depth of the groove ($\delta$) was 1 mm. Figure 1(b) shows the serial arrangement of the grooves at a 45-degree angle to the flow direction. An optimum depth-to-print diameter ratio, $\delta/Dp$, and pitch-to-depth ratio, $p/\delta$, of 0.5 and 9 were employed. This is represented in the Figure 1 with the X-coordinate showing the flow direction and the Y-coordinate showing the groove orientation arranged at 45°along the 203 mm width. Thus, the

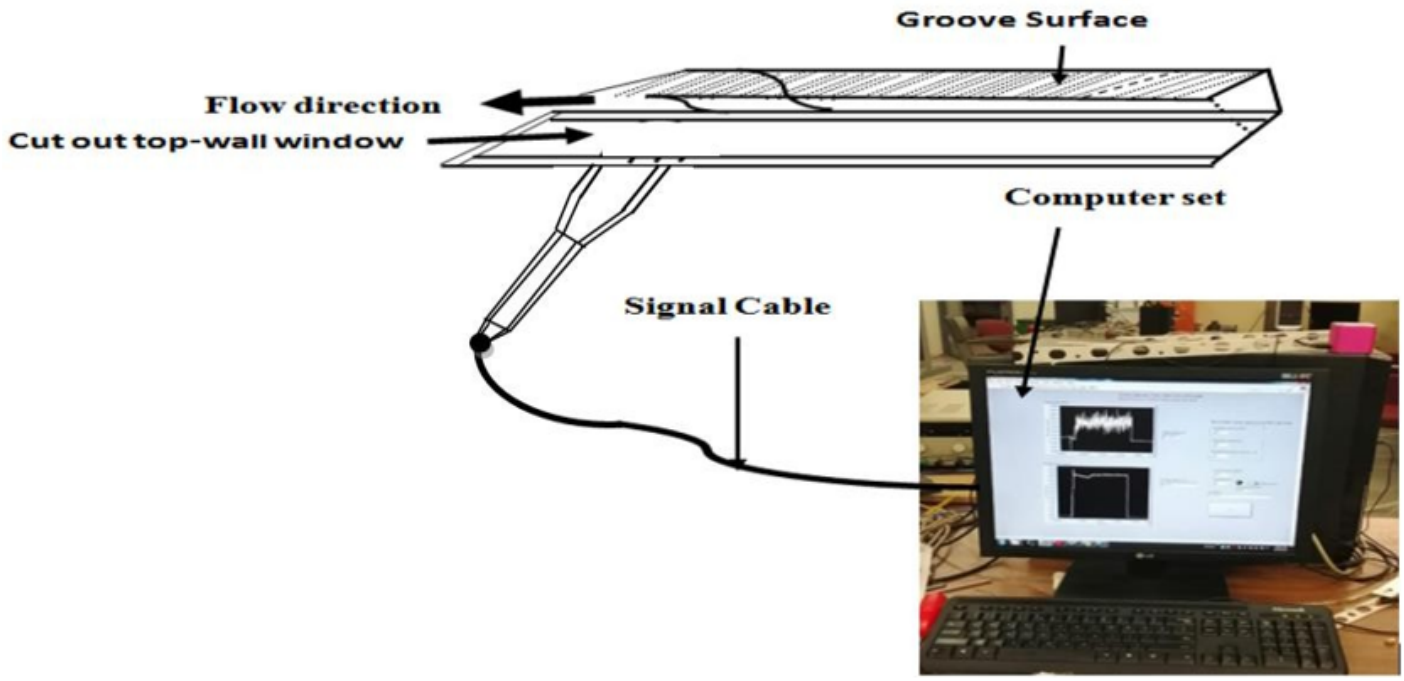


Figure 5. Thermal probe setup.

tests were conducted for three aspect ratios: 0.025, 0.0345, and 0.05. Using Eq. (3), the normalized static pressure drop was obtained for each of the Reynolds numbers presented Mahmood and Aasa [25]:

$$\Delta P^* = \frac{P_x - P_0}{0.5\,\rho_a\,U^2}. \tag{3}$$

The evaluation for friction factor was performed with a perfect line of fit curve at approximately 0.3 from the inlet of the test section, and the introduction of the groove was observed to proliferate the static wall pressure drop. The gradient ($\frac{\Delta P}{\Delta X}$), determined by the static wall pressure drop, is used in Equation 4 to express the friction factor

$$f = \frac{D_h\,(\Delta P_x/\Delta X)}{0.5\,\rho_a\,U^2}. \tag{4}$$

The side wall smooth surface is slotted in for thermal probe traverse and this is presented in Figure 3. This give opportunity to model the behaviour of flow upstream and downstream of the flow Figure 4 presented inbuilt thermal probe used to obtain the surface test section data to show the flow distribution within the channel. Eq. (5) presents the expression for surface effect of the groove endwall on the flow distribution within the section for the pressure coefficient, $Cp$loss,in detail of the set is presented in Figure 5.

$$C_{\text{ptloss}} = \frac{P_{\text{Tot}}}{0.5\,\rho_a\,U^2}. \tag{5}$$

The detailed arrangement of the thermal probe, traverse and acquisition computing setups are presented in Figure 5. The thermal probe assembly is thereafter affixed to the two-axis traverse system operated by a Velmex$^{\text{TM}}$ motor controller to conduct measurements along the channel's plane. The measurements were obtained at a flow cross-section 20 mm downstream of the test section exit. The thermal probe is a self-built setup that is fabricated internally in the laboratory and used for the measurement of the air temperature distribution within the heated channel. The tip of the probe was a butt-welded K-type thermocouple connected according to the principle described in Ref. [26]. It is then suspended in a long rod that securely holds it in place by hypodermic needles separated by 10 mm from the cable connected to the DAQ system through a 5 mm diameter hollow rod. The thermal probe was then calibrated with a thermal water bath to ensure consistency and determine the uncertainty. The thermal probe assembly was then finally installed with a two-axis transverse system driven by a Velmex$^{\text{TM}}$ motor controller for measurement scanning and acquisition along the plate. The developed LabVIEW program operated a probe at 60 Hz for 2 s to obtain the data. Using Equation 6, the non-dimensional temperature, $\theta$, is evaluated along the cut-out slot of the 203 mm wide wall dimension Liu *et al.* [27, 28]:

$$\theta = \frac{u\,T}{U\,T_{\text{tp,exit}}}, \tag{6}$$

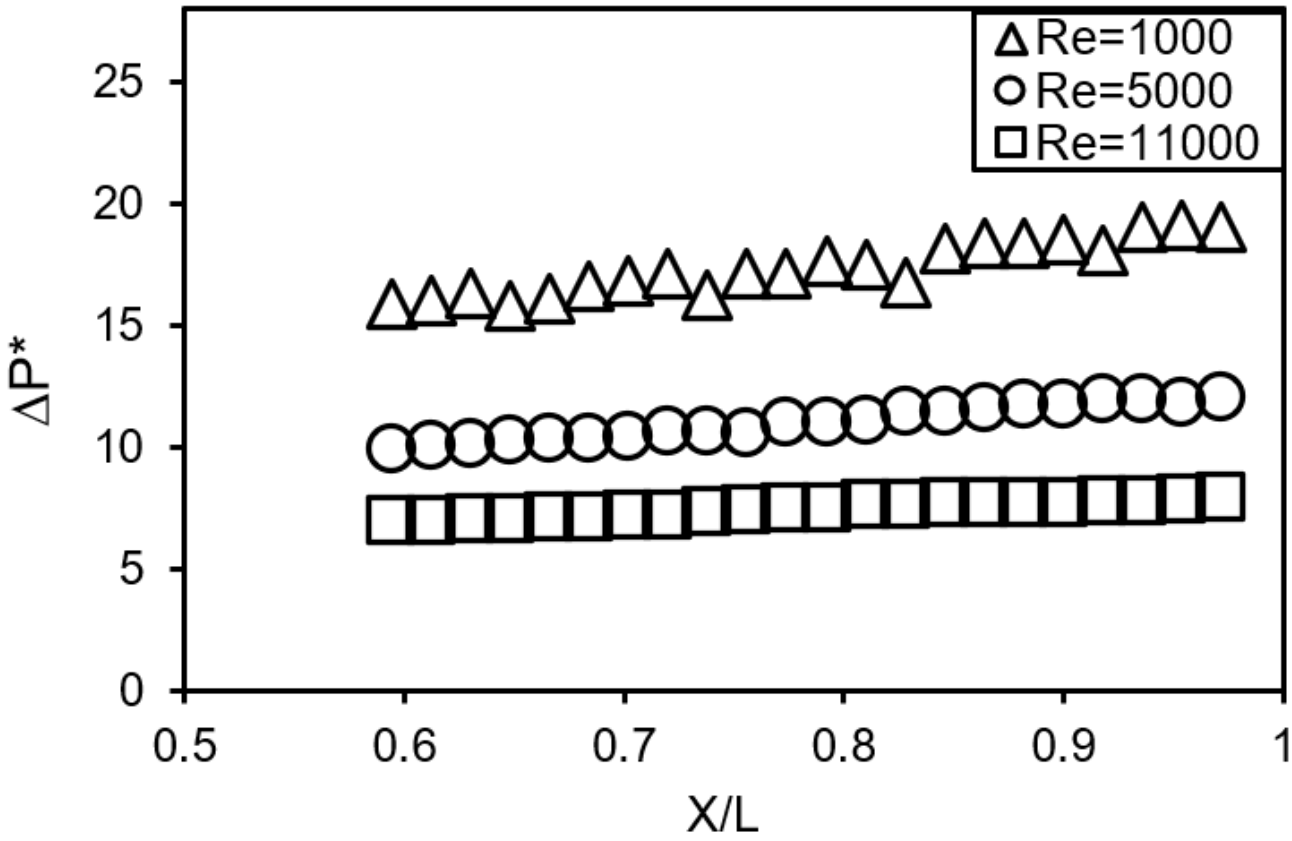


Figure 6. Normalized wall static pressure drops with and without groove versus normalized distance across test section.

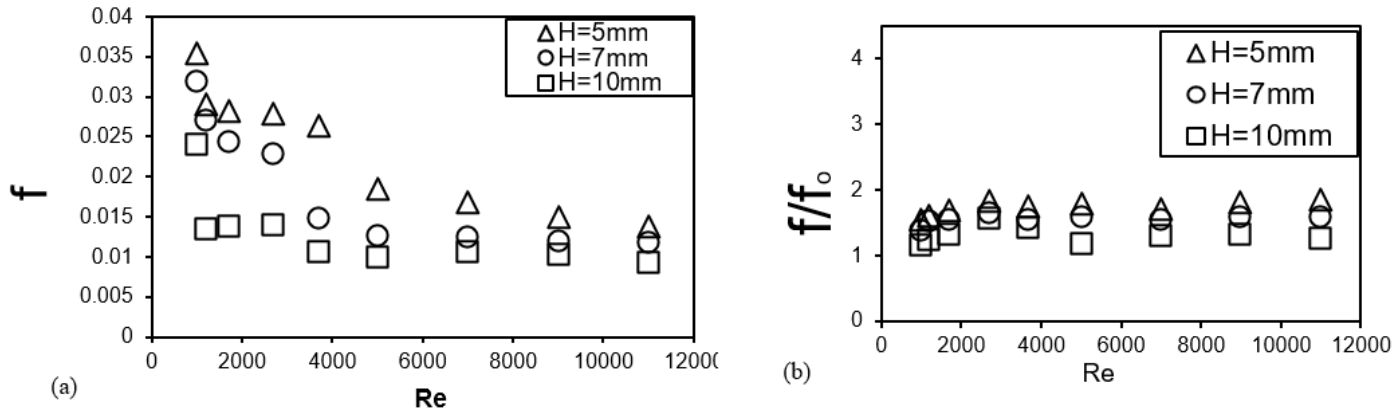


Figure 7. (a): Friction factor across the test section versus Reynolds number for 5 mm, 7 mm and 10 mm channel height (b) Friction factor ratio across the test section versus Reynolds number for 5 mm, 7 mm and 10 mm channel height.

where $u, T$ is the local stream wise velocity and measured temperature, $U, T_{m,exit}$ = average channel velocity for $Re$, and T is the bulk exit temperature. The scans were carried out along the width of the plate at 1 and 2 mm for 7- and 10-mm channel heights and 5 mm along the 203 mm width of the plate at each Re.

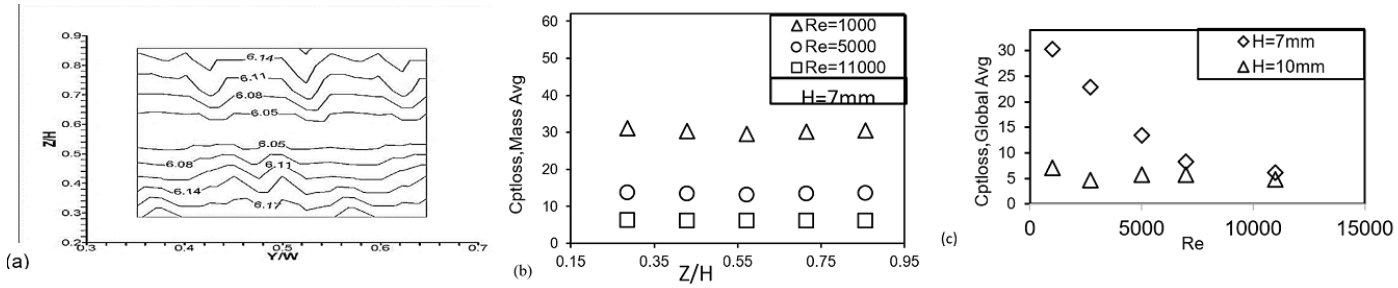


Figure 8. (a). $C_{ptloss}$ contour plot along the test section plane height, $Z/H$ and width, $Y/W$ for 7 mm channel. (b). $C_{ptloss}$, mass average versus the height, $Z/H$ and (c). $C_{ptloss}$, global average versus Reynold number.

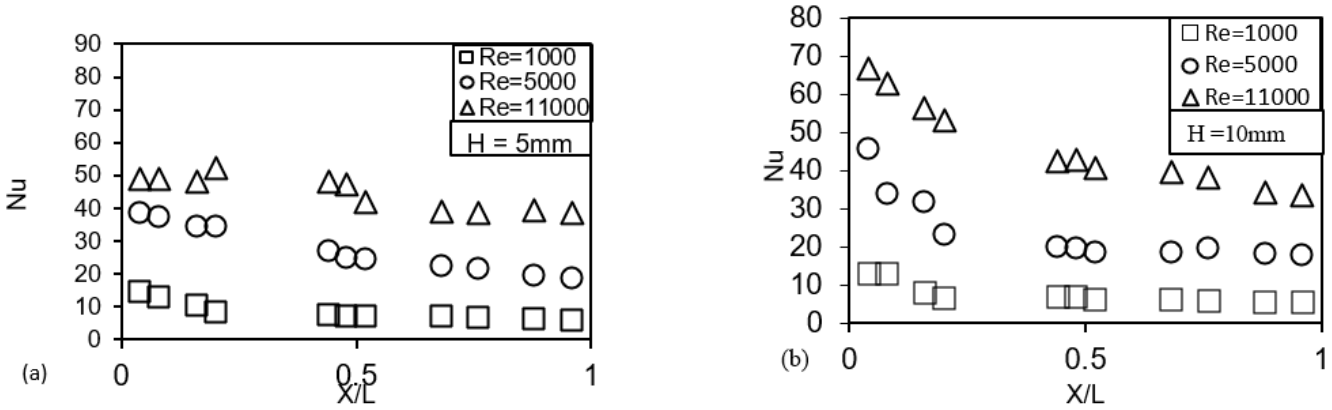


Figure 9. (a) Local Nusselt number along the mainstream of the test section for 5 mm channel and (b) local Nusselt number along the main stream of the test section for 10 mm channel height.

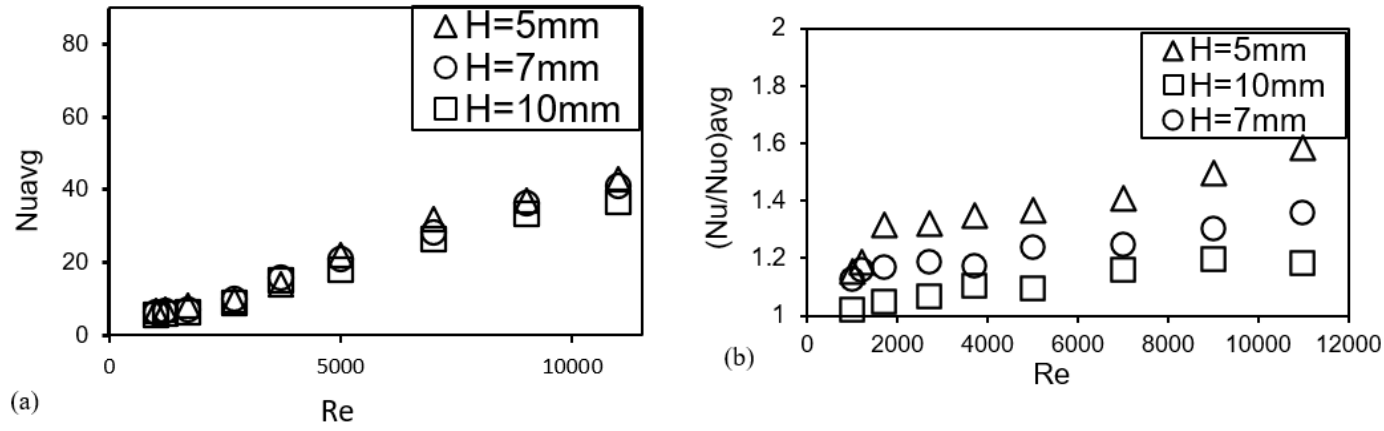


Figure 10. (a) Average local Nusselt number across test section against Re (b). Ratio of average local Nusselt number of the groove and smooth surface across the test section against Re.

### 2.3. *Uncertainty analysis*

The studies [26, 27, 29] assessed the uncertainties in the experimentally measured data using a 95% confidence interval. This indicated that the error in the experimental temperature measurements was 0.2°C, the uncertainty in Qc was 5%, and the uncertainty in the total heater power on a plate was 3% at Re = 1000 and 11,000, respectively. The uncertainty in the wall static pressure was 0.7 Pa at Re = 1000 and 5.8 Pa at Re = 11,000 at locations $\frac{X}{L} \geq 0.98$. The uncertainty in measuring the mass flow rate was 1%. The

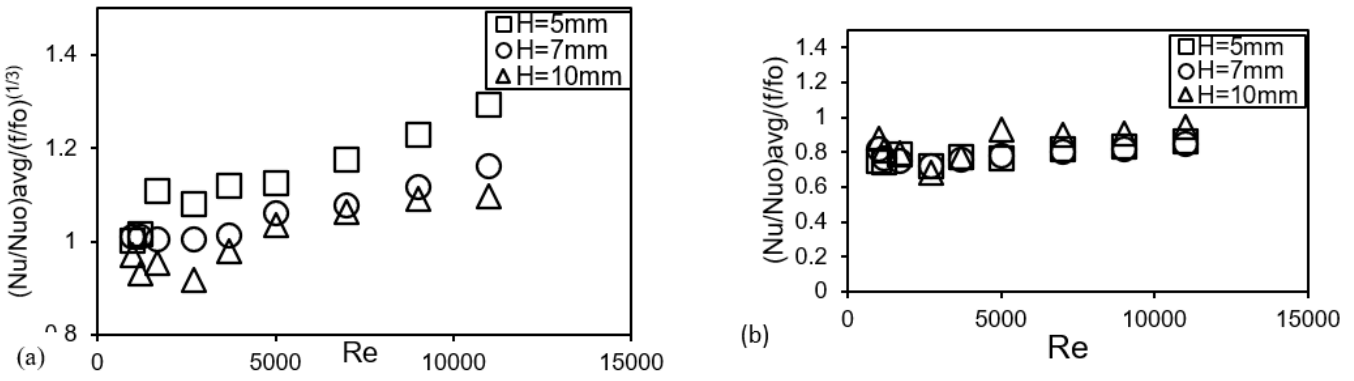


Figure 11. The thermal performance index: (a) $\frac{Nu/Nu_0}{(f/fo)^{1/3}}$ and (b) $\frac{Nu/Nu_0}{f/fo}$ of the groove test section as dependent upon Re for two.

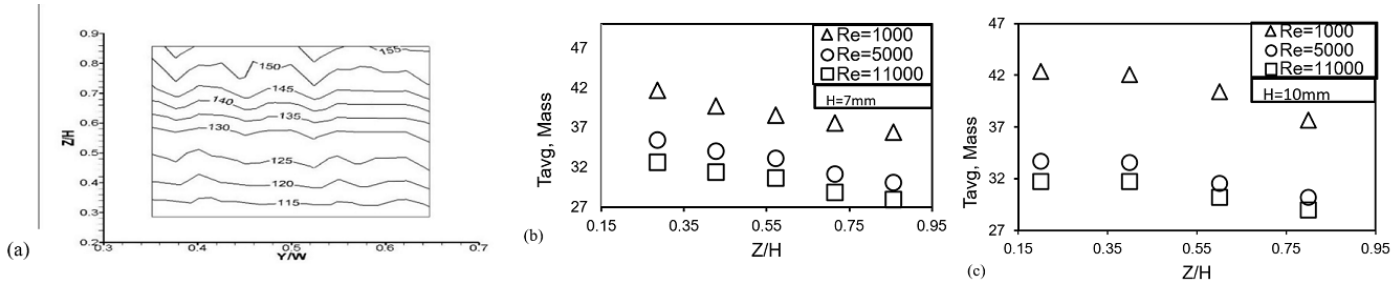


Figure 12. Test section exit air temperature for height ($Z/H$) and width ($Y/W$) (a) contour plot (b). Normalised pitch-averaged height for 7 mm, (c). Normalised pitch-averaged height for 10 mm.

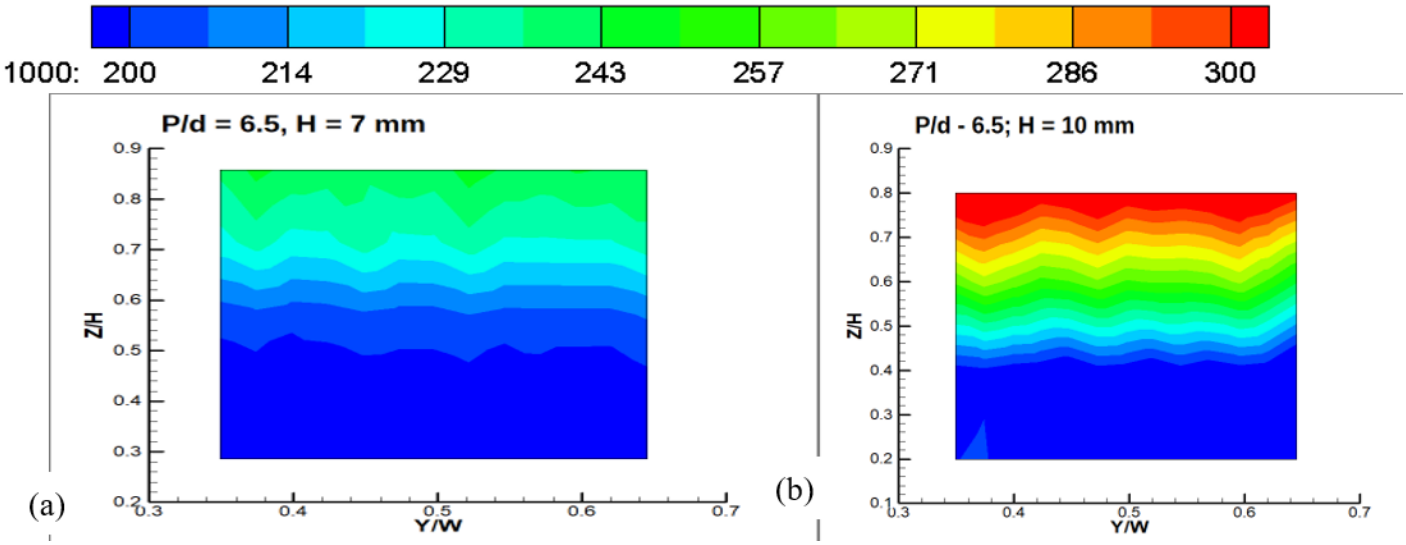


Figure 13. Surface weighted surface groove air-temperature at the exit of the test section for $\frac{P}{\delta}$ = 6.5 at 1000 Re (a) $H$ = 7 mm and (b) 10 mm.

uncertainty in the calculated f was 8% at Re = 1000 and 3% at Re = 11,000. The low pressure drop in the channel accounted for the high uncertainty in the friction factor at low Re. The calculated Nu had an uncertainty of 7% at Re = 1000 and 5% at Re = 11,000. Three samples were tested for each Reynolds number to account for data inaccuracy. The variations in the pressure drop and Nusselt number distributions were approximately 5%.

Table 1. Test ambient conditions.

| # | Ambient Parameters | Values |
|---|---|---|
| 1 | Temperature | 18–26 °C |
| 2 | Pressure | 86470–96704 Pa |
| 3 | Transducers (-0.5, 2.0, 5.0, 10.0) | 0.2–1.0 V |

Table 2. Experimental boundary condition.

| # | Re | $Q$ (W/m$^2$) | $T_w - T_{mx}$ (°C) | $Q_{cx}$ (W/m$^2$) |
|---|---|---|---|---|
| 1 | 630.00 | 20.00 | 12.00 | 19.30 |
| 2 | 1000.00 | 24.60 | 15.00 | 24.00 |
| 3 | 1200.00 | 26.00 | 16.00 | 25.40 |
| 4 | 3700.00 | 65.00 | 22.00 | 63.60 |
| 5 | 5000.00 | 108.00 | 21.00 | 105.60 |
| 6 | 7000.00 | 140.00 | 21.00 | 136.90 |
| 7 | 9000.00 | 154.00 | 19.00 | 150.60 |
| 8 | 11000.00 | 180.00 | 22.00 | 176.00 |

## 3. Results and discussion

Details of the pressure drop and heat transfer along the surface of the mainstream of the channel were measured and reported. The data was collected when the test conditions were stable, meaning the temperature and pressure drop changed by less than 0.05-0.1°C and 2.5 Pa, respectively. The steady state was reached at about 10 – 15 minutes after the facility started. Tests were performed for Re = 1000, 5000, and 11000. Based on the properties of the fluid used, a total velocity of less than 20 ms$^{-1}$ and 5.0 kPa and a surface temperature of approximately 55°C, the system is said to be incompressible. Two-wall heated and one-wall heated test measurements of the heat transfer were performed while the other was kept adiabatic. Table 1 enlists the test conditions for all measurements. The heat flux in the Table 2 is based on the average convective heat flux from the heated wall. Air viscosity and density ($\mu a$, $\rho a$) were estimated at $T_{a,\text{in}}$. Following the experimentation the boundary conditions applicable for this study is presented in Table 2. The Reynolds numbers, Re, ranges from 630 – 11000 was tested and corresponding flow conditions of air velocity and heat flux are applied to the bottom section of the test area. The heat flux are noticed to varied from 20 to 180 W/m$^2$. Also the corresponding convective heat flux along the endwall was measures to vary from 19.20 – 176 W/m$^2$, a maximum variation less that 4% are observed in the laminar and less than 2.5% in the fully developed regimes. The mix mean temperature are also observed to be higher than 10°C (Figures 3 to 6).

### 3.1. Pressure drop measurement

The normalized static pressure drop coefficients $\Delta P$ along the $X/L$ direction are shown for a channel height of 5 mm at Re = 1000, 5000, and 11000 in Figure 6. The reference pressure P0 in the equation was obtained 10 mm upstream from the test section inlet on the test wall. The Re for the data in Figure 6 covers the laminar to turbulent flow regimes. The figure shows the normalized static pressure drop of $\Delta P*$ against $X/L$ as Re increases and the decrease in $\Delta P*$ along the $X/L$ direction. The distribution of normalized static pressure, $\Delta P*$, at different Re values in Figure 6 is a straight line from 0.0 to 1.0 for $X/L$ and does not clearly show where the flow changes to fully developed flow in the test channel.

### 3.2. Friction factor analysis

Figure 7(a) displays the results of the friction factor, $f$, across the entire range of Re, 1000-11000, in the tests. For channel heights of 5, 7, and 10 mm, the friction factor decreased as the Re number increased. The friction factors were 0.035 and 0.0137 for a 5 mm channel height with an aspect ratio of 0.025 and Re numbers of 1200 and 11000, respectively. These friction factors have the greatest effect when compared with the aspect ratios of 0.0345 and 0.05 channel heights in the experiments. Figure 7(b) presents the ratio of the groove to the smooth channel friction factors for Re 1000-11000. The results for the friction factor ratio indicate that the introduction of the grooves increases the pressure drop to 1.16–1.25 times for the 10 mm, 1.37–1.6 times for the 7 mm, and 1.5–1.85 times for the 5 mm channel heights, respectively. In addition, the friction factor increases steadily until it reaches Re 2700, after which it drops and rises gradually again to the last Re of 11000, which gives the highest ratio. Figure 8(a) illustrates how the profile of the pressure surface changes as the $p_{tot}$ tube collects data from 3 mm to the end of the test section, measuring from the bottom to the top of the channel in 1 mm steps vertically and 5 mm steps horizontally. The plot shows that the distribution along the surface of the groove was uniform, indicating an even flow of fluid in the channel. In addition, the pressure distribution decreased as the tube moved away from the surface of the groove and increased gradually as it reached the smooth top wall. Figure 8(b) shows the average pressure coefficient at different points along the groove channel for a channel height of 7 mm and Re values of 1000, 5000,

and 11000. From the graph, a gradual fluid flow distribution along the channel was observed, and a prominent effect of the groove was observed toward its wall, approximately 31.2 Pa, compared to a smooth top wall that reads approximately 30.3 Pa at Re 1000.

A slight reduction in the pressure distribution at the center of the channel indicates a smaller effect of the groove. The same phenomenon is replicated in all other Reynolds numbers, Re, 5000, and 11000; a 2-3% difference is noticed from the bottom groove wall to the top smooth wall. Figure 8(c) presents the global mass average pressure coefficient for the 10 mm and 7 mm channel heights and Re 1000-11000. The plots indicate the distribution, with Re 1000 having the highest Cpt and 11000 being the lowest. A gradual distribution is observed just before the transition stage of 2700 to 5000, which gives a shape flow distribution and returns to normal from 7000 to 11000. This plot indicates that a prominent effect of the groove is observed at high Reynolds numbers compared with the lower ones.

### *3.3. Nusselt number*

Figure 9(a) displays the local Nusselt number, $Nu_x$, for the channel height of 5 mm. The Nusselt number is shown on a graph with the thermocouple position, $X/L$, and it clearly indicates that the flow is fully developed at about 0.3 of the test section for all Reynolds numbers of 1000, 5000, and 11000. The Nusselt numbers were all on the plate's smooth surface, with no thermocouple in the groove. The low uncertainty of the local Nusselt number was maintained by ensuring that the difference between the wall and the mix-mean temperature was approximately 10°C. The supplied heat flux is dependent on Re in the channel and the applicable channel height. The local Nusselt numbers of the repeated tests only varied by 3% along the $X/L$ direction. A decrease in the Nusselt number was observed immediately before the fully developed regions: $X/L \leq 0.6$, after which a steady state was reached, which indicates a fully developed thermal system. The system's local Nusselt number and Nux distribution increase as the Re in the system increases, reaching values of 7.4, 24.6, and 53.9, respectively, at $X/L = 0.98$. In Figure 9(b), the local Nusselt number, $Nu_x$, starts off high at the beginning of the test section and then becomes steady in the thermally developed section when $X/L$ is 0.6 or more, with values of 6.4, 22.6, and 36.1 for Re 1000, 5000, and 11000, respectively, at $X/L = 0.98$. Figure 10(a) presents the average Nusselt number, Nuavg, for all Re 1000-11000. Averaging was performed from location $X/L \approx 0.6$. The average Nusselt number, Nuavg, increases as Re increases for all channel heights tested. An incremental difference of 8-9% exists between the aspect ratios 0.025, 0.0345, and 0.05 Re 1000-3700, and a maximum of 15% exists between Re 5000-11000. The average ratio of Nusselt numbers for grooves compared to smooth channels, $Nu_{avg}/Nu_0$, is illustrated in Figure 10(b) based on the average Nusselt numbers calculated for channel heights of 5, 7, and 10 mm. For a channel height of 5 mm, a maximum increase of 86% was observed at Re 11000 and a minimum of 50% at the smallest Re of 1000; a 7 mm channel height gives a 33% increment at Re 1000 and 73% for Re 11000, while 10 mm has an incremental change of 21% at Re 1000 and 61% at Re 11000. Therefore, even with a moderate pressure drop, the system operation benefits from the groove enhancement. This plot shows the three aspect ratios tested; the 0.05 aspect ratio gives the highest effect of the groove. This experiment yielded similar results to those of the angled groove with a large pitch, as reported by Saha and Acharya [30]. Figure 11(a) shows the overall thermal performance, $\frac{Nu/Nu_0}{(f/f_0)^3}$, of the three channel heights performed in this experiment for Re 1000-11000.

The variation between Re is evenly varied between Re 1000 and 1700, after which a nominal difference was noticed for Re 2700-5000; then, it dropped a bit and increased gradually throughout the turbulence region of Re 7000-11000. The highest effect of the flow was observed for the 5 mm channels; the 7 mm and 10 mm channel heights had the least effect on the groove. The performance index, studies by [30–32], shows thermal performance values of 1.15-1.4 for 10 mm, 1.2-1.48 for 7 mm, and 1.3-1.58 for 5 mm, within the Reynolds number range of 900 to 13000. Figure 11(b) presents the efficiency index, $\frac{Nu/Nu_0}{f/f_0}$, of the three channel heights, which represents the ratio of the heat enhancement coefficient to the groove friction factor when compared with the smooth channel. The category of these efficiencies decreased as Re increased from 1000 to 2700. A slight reduction is detected from Re 2700 to 7000 and gradually picks up for higher Reynolds numbers, with a maximum of 1.2 reached at 10 mm height and Re 11000. The effect of the grooves was minimal throughout the lamina and transition region compared to the turbulence region. Others replicate this procedure with channel heights of 7 mm and 5 mm, achieving efficiency values of 1.08 and 1.01 at Re 11000. The temperature profile distribution for a channel height of 7 mm at 10 mm from the exit of the test section. The thermal probe used was made from a T-type thermocouple with a tip of 10 mm oriented at a 90° angle to the long arm, which is attached to the traverse system. Figure 12(a) shows that a uniform temperature motion occurs throughout the channel height, particularly when the data point location is considered. However, the groove's effect is more pronounced near its surface compared to the top smooth surface, which displays a significantly higher temperature. The mass average for a Figure 12(b) presents the mass average for a channel height of 7 mm for Re = 1000–11000. The average temperature increases down the surface, specifically across the channel height, as depicted in Figure 13(a). Changes of 14%, 16%, and 16% were seen from the end wall to the groove surface and top wall for laminar, transition, and turbulence conditions, respectively. Furthermore, the same pattern is shown in Figure 12(c), where the average temperature increases along the channel by 9%, 11%, and 13% for laminar, transitional, and turbulence conditions, respectively. These results show that the groove is more effective in the flow with a smaller channel height.

### *3.4. Air temperature distribution*

The air temperature at the exit of the test section was determined to provide a more detailed overview of the flow distribution in the channel. Following Eq. (6), Figures 13 to 15 show the air temperature distribution along the channel width for 7 mm (0.034

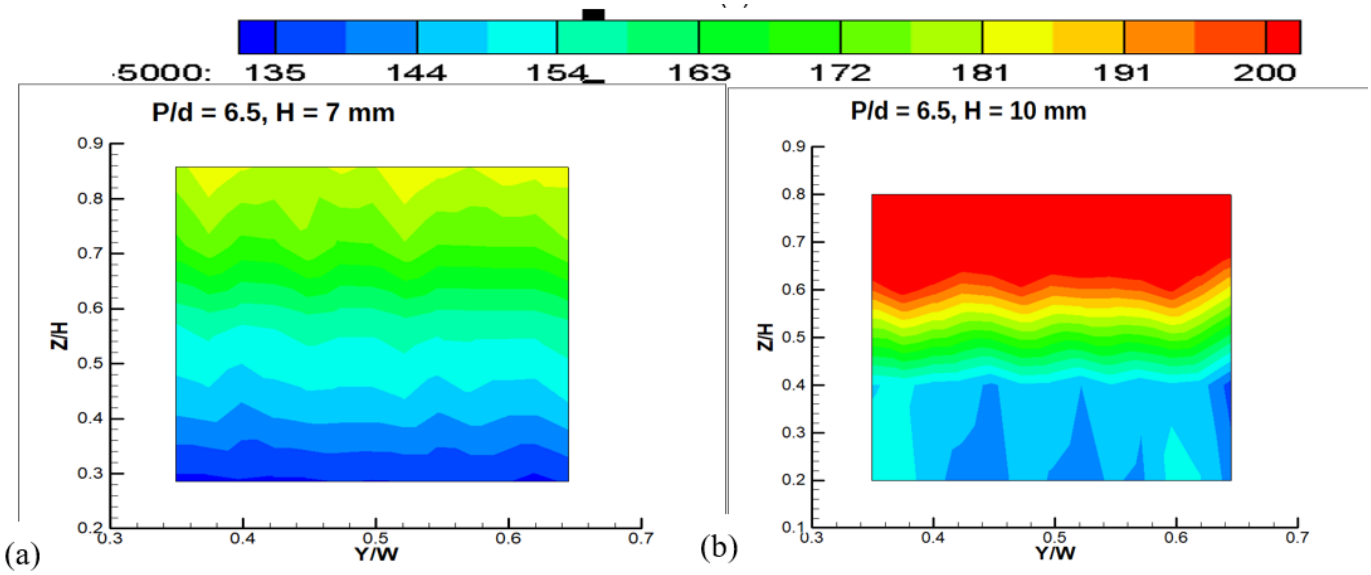


Figure 14. Surface weighted surface groove air-temperature at the exit of the test section for $\frac{p}{\delta} = 6.5$ at 5000 Re (a) $H = 7$ mm and (b) 10 mm.

aspect ratio) and 10 mm (0.05 aspect ratio). An overview of the air distribution of the thermal surface along the control volume of the groove plate is provided as follows: The data were obtained at 10 mm near the exit of the test section. The data were obtained from the surface of the groove wall to the smooth top wall along the $Y/W$-direction and through the centrally located slot in the $Z/H$-direction along the width of the plate. The stepper motor was configured to travel along the $Y/W$ direction at 1 mm and 2 mm intervals at 7 mm (0.034 aspect ratio) and 10 mm (0.05 aspect ratio) channel heights, respectively. Following the successive thermal probe setup, it was calibrated to improve data accuracy. The temperature distribution in the control volume was monitored over the range of $1000 \leq Re \leq 11000$. Figure 14 shows the air temperature pattern for Re 1000 and groove plate numbers, $\frac{p}{\delta} = 6.5$ mm, at a channel height of 7 mm in Figure 13(a), while Figure 13(b) shows the same for a channel height of 10 mm. The figures illustrate how the flow is spread out in the control area with a low mixing rate, having a 0.034 aspect ratio; Figure 13(a) shows that the flow is more evenly spread due to the grooves helping to move the flow, resulting in a lower temperature compared to Figure 13(b), where the flow is less even and has higher temperatures. When the experiments were done using groove plates with $P/\delta = 9$ mm and $P/\delta = 13$, the plates caused less mixing because of how the grooves were arranged, the pumping power they created, and the low turbulence in the channel. Figure 14 illustrates the air temperature near the exit of the test section for groove plates $P/\delta = 6.5$ at channel heights of $H = 7$ mm (0.034 aspect ratio) and 10 mm (0.05 aspect ratio) at Re 5000. This figure indicates that the transition regime of the flow distribution was affected by the groove arrangement.

An irregular distribution is observed in all the groove aspect ratios in the transition regime, where the flow is readily prepared to move to the turbulence regime; owing to irregularities in pumping effects, many fluctuations are observed. Notably, the flow distribution improved as the aspect ratio reduced from 0.05 to 0.035 at the same Reynolds number (Re). Thus, the flow pumping power was more efficient at an aspect ratio of 0.035 compared to 0.05, thereby influencing the rate of enhancement. Figures 15(a) and (b) display the air temperature near the exit of the test section for groove plates with a $P/\delta$ ratio of 6.5 at channel heights of 7 mm (0.034 aspect ratio) and 10 mm (0.05 aspect ratio) at a Reynolds number of 11000. These figures indicate that the transition regime of the flow distribution was affected by the groove arrangement. A more uniform distribution was observed in all groove aspect ratios during the turbulent flow experiment owing to the high pumping capacity. Note that as the Reynolds number increased, the flow turbulence increased, and the cooling rate increased as the aspect ratio decreased. The flow pumping power was more effective at an aspect ratio of 0.034 ($H = 7$ mm channel height) than at a 0.05 aspect ratio (10 mm channel height), as indicated by the cooling rate. As the pumping power increased, the groove's effect on fluid distribution became more noticeable. The increased effect of aerodynamic drag on the fluid and its high turbulence ratio make mixing it inexpensive. The recorded air temperature spread at the end of the channel shows how well the cold and hot fluids mix due to the grooves and how deep the mixing goes along the height of the channel. A uniform air temperature distribution and mixing intensity between the cold and hot fluids is always desirable across the flow section at the heat-exchanger channel exit. The aspect ratio is clearly a major factor; as it decreases, an increase in pumping power is observed with the impact of the groove and the turbulence ratio. As a result, the channel aspect ratio of 0.34 has an improved mixing rate, resulting in much lower temperatures than the respective Reynolds numbers in the 10 mm channels. A range of 50 – 315, 30 – 240, and 28 – 200 was observed for Re 1000, 5000, and 11000, respectively, for both 7 mm and 10 mm channel heights. The grooved plate $\frac{p}{d} = 6.5$ proved to be the most effective with the highest cooling rate for all Reynolds numbers.

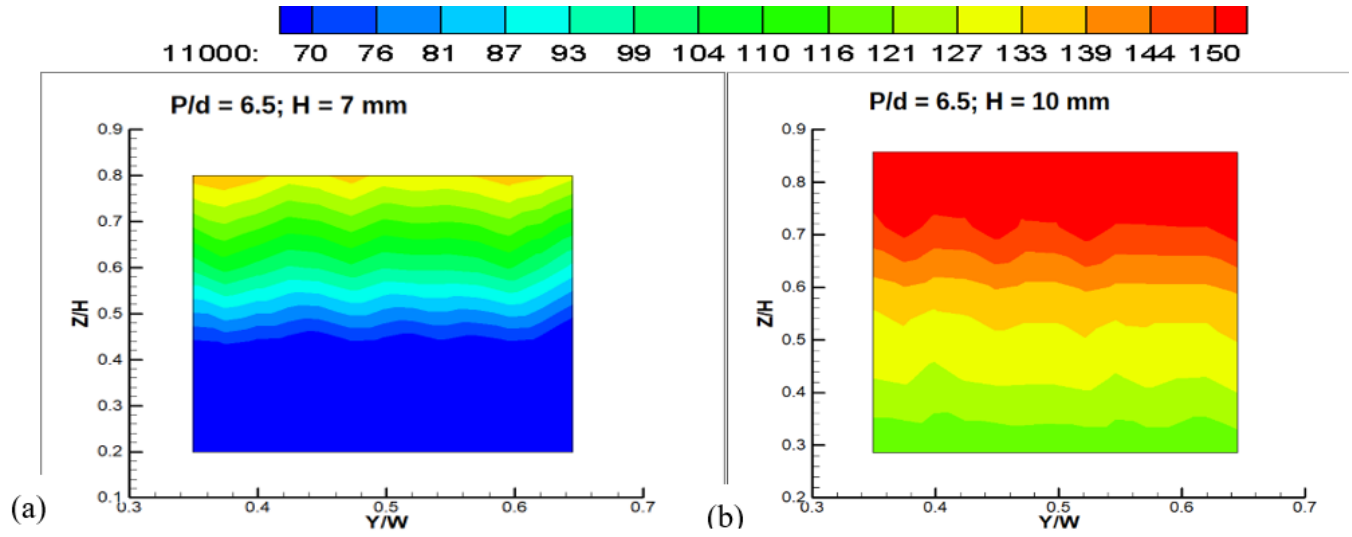


Figure 15. Surface weighted surface groove air-temperature at the exit of the test section for $\frac{P}{\delta}$ = 6.5 at 11000 Re (a) $H$ = 7 mm and (b) 10 mm.

## 4. Conclusion

These data, which are obtained in a rectangular channel, are used to determine the optimal behaviour and performance of several parameters, including the friction factors, Nusselt number, pressure loss coefficient, mass average, and heat transfer coefficients, in a semi-circular groove that is periodically prescribed. The groove, which covered 203 × 500 mm of the test section length utilised for three distinct aspect ratios of 0.025, 0.034, and 0.05, was angled at 45°, 1 mm depth, and 9 mm pitch. Only one side of the channel's groove surface was used; the other side was left flat, and only the grooved wall provided the data. The heater was fastened to the wall's grooved, smooth surface. In this study, the Reynolds values were fixed between 1000 and 11000. In this experiment, a common use of artificial enhancement in fuel cells, solar cells, photovoltaic cells, and internal turbine vane cooling was reproduced. The following are the conclusions drawn from the measurements

i The arrangement of the grooves affects the flow edifices, and it is further established that the spacing, orientation angle, rational configuration, and impingement rate of the grooves all have important effects.

ii The friction factor f and friction factor ratio $f/f_0$ in the channel determine the dependent parameter ReDh. An increase in the friction factor is observed as the Reynolds number increases, for the range of f/f0 ratio increases with Re ≤ 2700, after which it drops slightly for Re = 2700 to Re = 5000. The range of observed values of the friction facto ratio is 1.43 to 2.59. The highest impact of the groove was felt for an aspect ratio of 0.025. This is similar to what Saha and Acharya [11].

iii For the 5 mm channel with an aspect ratio of 0.025, the enhanced heat transfer, $Nu_{avg}/Nu_o$, was the highest. As ReDh increased for each channel, the ratio of Nusselt number for 2700≥ReDh≤5000 decreased and then began to increase throughout the turbulence region.

iv The surface temperatures of the aspect ratios demonstrate that a temperature gradient is detected from the groove end to the smooth top wall. In addition, the temperature of the smooth wall is higher than that in the middle of the channel. This demonstrates that the wall influences flow in the channel.

v The pressure drops coefficients at the exit of the channel, as affected by the groove arrangement, are presented, along with the flow structure in the channel with the lowest pressure drop at the middle of the channel and the highest surface of the groove. From the presented figures, a global $C_{\text{ptloss}}$ of 30 to 6 is observed for 7 mm channels and a range of 7 to approximately 5 for 10 mm channel height.

## Nomenclature

| | |
|---|---|
| $A_c, D_h$ | channel cross-sectional area, hydraulic diameter |
| $C_p, k_a$ | specific heat, thermal conductivity of air |
| $F$ | friction factor in screen channel |
| $H, L, W$ | height, length, width of test section |
| $m_a$ | mass flow rate of air |
| Nu | Nusselt number |
| $P_x, P_0, P^*$ | Pressure: local wall-static, reference, normalized on wall |
| $Q_c, Q_{c,x}$ | total convective power, local convective power on surface |
| Re | Reynolds number, $\left(\frac{M_a D_h}{A_c \mu_a}\right)$ |
| $T_{a,\text{in}}, T_{m,x}, T_{w,x}$ | Temperature: inlet air, local bulk-mean of air, on wall at distance $x$ |
| $U$ | mean flow velocity, $\left(\frac{m_a}{A_c \rho_a}\right)$ |
| $X, Y, Z$ | Cartesian coordinate system |
| $C_{\text{ptloss}}$ | Coefficient of total pressure loss |
| $P_{\text{Tot}}$ | Total Pressure |
| $\Delta$ | difference between two quantities |
| $\mu_a, \rho_a$ | dynamic viscosity, density of air |
| Avg | Average |
| $x$ | local property on the wall along $x$ |
| 0 | reference or smooth channel property |
| $\Theta$ | Non-dimensional Temperature |

## Data availability

The datasets generated and analyzed during the current study are available from the corresponding author on reasonable request.

## References


[1] S. A. Solovitz & T. E. Conder, "Flow and thermal investigation of a grooved-enhanced minichannel application", Journal of Thermal Science and Engineering Applications **2** (2010) 1. https://doi.org/10.1115/1.4002411.

[2] E. H. Ridouane & A. Campo, "Heat transfer enhancement of air flowing across grooved channels: joint effects of channel height and groove depth", Journal of Heat Transfer **130** (2008) 1. https://doi.org/10.1115/1.2790022.

[3] P. L. Sharma, D. Bais & P. Thakur, "Thermal instability of rotating Jeffrey nanofluids in porous media with variable gravity", Journal of the Nigerian Society of Physical Sciences **5** (2023) 1366. http://dx.doi.org/10.46481/jnsps.2023.1366.

[4] S. O. Salawu, R. A. Kareem & J. O. Ajilore, "Eyring-Powell MHD nanoliquid and entropy generation in a porous device with thermal radiation and convective cooling", Journal of the Nigerian Society of Physical Sciences **4** (2022) 924. http://dx.doi.org/10.46481/jnsps.2022.924.

[5] M. Arik & R. S. Bunker, "Electronics packaging cooling: technologies from gas turbine engine cooling", ASME Journal of Electronic Packaging **128** (2006) 215. https://doi.org/10.1115/1.2229219.

[6] P. J. Pretorius, G. I. Mahmood & J. P. Meyer, "Static pressure characteristics in pin fin channel with cylindrical pins", ASME Journal of Fluids Engineering **139** (2017) 091104. https://doi.org/10.1115/1.4036671.

[7] G. I. Mahmood, C. J. Simonson & R. W. Besant, "Experimental pressure drop and heat transfer in a rectangular channel with a sinusoidal porous screen", ASME Journal of Heat Transfer **137** (2015) 042601. https://doi.org/10.1115/1.4029349.

[8] O. A. Oyekanmi, S. Amole, O. Akinrinola, O. Adedokun, A. K. Dauda, F. A. Ojeniyi & A. O. Awodugba, "Reduced graphene oxide as the electron transport layer in perovskite solar cell: Effect on the photovoltaic performance", Recent Advances in Natural Sciences **2** (2024) 116. https://doi.org/10.61298/rans.2024.2.2.116.

[9] P. M. Ligrani, J. L. Harrison, G. I. Mahmood & M. L. Hill, "Flow structure due to dimple depressions on a channel surface", Physics of Fluids **13** (2001) 3442. https://doi.org/10.1063/1.1404139.

[10] G. I. Mahmood, M. Z. Sabbagh & P. M. Ligrani, "Heat transfer in a channel with dimples and protrusions on opposite walls", Journal of Thermophysics and Heat Transfer **15** (2001) 275. https://doi.org/10.2514/2.6623.

[11] K. Bilen Cetin, M. Gul & T. Balta, "The investigation of groove geometry effect on heat transfer for internally grooved duct", Applied Thermal Engineering **29** (2009) 753. https://doi.org/10.1016/j.applthermaleng.2008.04.008.

[12] P. S. Lee and C. J. Teo, "Heat transfer enhancement in microchannels incorporating slanted grooves", in *Proceedings of the International Conference on Micro/Nanoscale Heat Transfer*, vol. 42924, pp. 819–823, 2008. https://doi.org/10.1115/MNHT2008-52374.

[13] Y. Xie, Z. Shen, D. Zhang & J. Lan, "Thermal performance of a water-cooled microchannel heat sink with grooves and obstacles", Journal of Electronic Packaging **136** (2014) 021001-1. https://doi.org/10.1115/1.4025757.

[14] E. Eiamsa-ard & P. Promvonge, "Thermal characteristics of turbulent rib-grooved channel flow", International Communications in Heat and Mass Transfer **36** (2009) 705. https://doi.org/10.1016/j.icheatmasstransfer.2009.03.025.

[15] T. E. Conder & S. A. Solovitz, "Computational optimization of a groove-enhanced minichannel", Heat Transfer Engineering **32** (2011) 876. https://doi.org/10.1080/01457632.2011.548632.

[16] P. M. Ligrani, G. I. Mahmood, J. L. Harrison, C. M. Clayton & D. L. Nelson, "Flow structure and local Nusselt number variation in a channel with dimples and protrusions on opposite walls", International Journal of Heat and Mass Transfer **44** (2001) 4413. https://doi.org/10.1016/S0017-9310(01)00101-6.

[17] W. M. Kays & M. E. Crawford, *Convective heat and mass transfer*, 3rd ed., McGraw-Hill Inc., USA, 1993. https://www.amazon.com/Convective-transfer-McGraw-Hill-mechanical-engineering/dp/0070334579/ref=monarch_sidesheet_title.

[18] J. Liu, G. Xie & T. W. Simon, "Turbulent flow and heat transfer enhancement in rectangular channels with novel cylindrical grooves", International Journal of Heat and Mass Transfer **81** (2015) 563. https://doi.org/10.1016/j.ijheatmasstransfer.2014.10.021.
[19] International Standard, ISO 5167-1980(E). (1980, July 15). *Measurement of fluid flow by means of orifice plates, nozzles and venturi tubes inserted in circular cross-section conduits running full* [Online]. Available: https://cdn.standards.iteh.ai/samples/11168/579951b09e254752a0b35aca5b78838b/ISO-5167-1980.pdf.
[20] R. K. Ravix & R. P. Saini, "Experimental investigation on performance of a double pass artificial roughened solar air heater duct having roughness elements of the combination of discrete multi V-shaped and staggered ribs", Energy **116** (2016) 507. https://doi.org/10.1016/j.energy.2016.09.138.
[21] R. L. Webb & N. H. Kim, *Principles of enhanced heat transfer*, 2nd ed., Taylor and Francis, New York, USA, 2005. https://doi.org/10.1201/b12413.
[22] R. K. Shah & A. L. London, *Laminar flow forced convection in ducts*, Academic Press, New York, 2014. https://www.sciencedirect.com/book/monograph/9780120200511/laminar-flow-forced-convection-in-ducts.
[23] R. J. Moffat, "Describing the uncertainties in experimental results", Experimental Thermal and Fluid Science **1** (1988) 3. https://doi.org/10.1016/0894-1777(88)90043-X.
[24] T. G. Beckwith, R. D. Marangoni & J. H. Lienhard, *Mechanical measurements*, sixth ed., Pearson Prentice Hall, New Jersey, 2015, pp. 42–45. https://link.springer.com/book/10.1007/978-3-030-73620-0.
[25] G. I. Mahmood & A. Samson, "Internal groove influenced thermohydraulic performance on an air-channel", in *Proceedings of the ASME Fluids Engineering Division Summer Meeting*, vol. 51555, V001T05A002, American Society of Mechanical Engineers, 2018. https://doi.org/10.1115/FEDSM2018-83236.
[26] S. Han & R. J. Goldstein, "Heat/mass transfer analogy for simulated turbine blade", International Journal of Heat and Mass Transfer **51** (2008) 5209. https://doi.org/10.1016/j.ijheatmasstransfer.2008.04.002.
[27] Y. Liu, J. Cui, W. Li, & N. Zhang, "Effect of surface microstructure on microchannel heat transfer performance", Journal of Heat Transfer **133** (2011) 1. https://doi.org/10.1115/1.4004594.
[28] P. Bharadwaj, A. D. Khondge & A. W. Date, "Heat transfer and pressure drop in a spirally grooved tube with a twisted tape insert", International Journal of Heat and Mass Transfer **52** (2009) 1938. http://dx.doi.org/10.1016/j.ijheatmasstransfer.2008.08.038.
[29] S. C. Lau, R. D. McMillin & J. C. Han, "Heat transfer characteristics of turbulent flow in a square channel with angled discrete ribs", Journal of Turbomachinery, **113** (1991) 367. https://doi.org/10.1115/1.2927885.
[30] K. Saha & S. Acharya, "Heat transfer enhancement using angled grooves as turbulence promoters", Journal of Turbomachinery **136** (2014) 081004-10. https://doi.org/10.1115/1.4025733.
[31] O. Abouali & N. Baghernezhad, "Numerical investigation of heat transfer enhancement in a microchannel with grooved surfaces", Journal of Heat Transfer **132** (2010) 1. https://doi.org/10.1115/1.4000862.
[32] R. L. Webb & N. H. Kim, *Principles of enhanced heat transfer*, second ed., Taylor and Francis, New York, USA, 2004. https://doi.org/10.1201/b12413.